Chemical Engineering Journal 465 (2023) 142907

Contents lists available at ScienceDirect

Chemical Engineering Journal

journal homepage: www.elsevier.com/locate/cej

Tailored interface composition improves the integrity of electrode/electrolyte interphases for high-voltage Ni-rich lithium metal batteries in a sulfolane-based electrolyte

Xiaodie Deng [a], Jialin Li [a], Pengbin Lai [a], Silan Kuang [a], Jiaxiang Liu [b], Pengpeng Dai [a], Haiming Hua [a], Peng Dong [c,*], Yingjie Zhang [c], Yang Yang [a,*], Jinbao Zhao [a,*]

[a] College of Chemistry and Chemical Engineering, State-Province Joint Engineering Laboratory of Power Source Technology for New Energy Vehicle, State Key Laboratory of Physical Chemistry of Solid Surfaces, Engineering Research Center of Electrochemical Technology, Ministry of Education, Collaborative Innovation Center of Chemistry for Energy Materials, Xiamen University, Xiamen 361005, P. R. China

[b] College of Energy, Xiamen University, Xiamen 361102, Fujian, China

[c] National and Local Joint Engineering Laboratory for Lithium-ion Batteries and Materials Preparation Technology, Key Laboratory of Advanced Battery Materials of Yunnan Province, Faculty of Metallurgical and Energy Engineering, Kunming University of Science and Technology, Kunming 650093, China

ARTICLE INFO

Keywords:
High voltage
Lithium metal batteries
Sulfone-based electrolytes
Ni-rich cathodes
Electrode/electrolyte interphases

ABSTRACT

High-voltage lithium metal batteries (LMBs) matched with Ni-rich cathodes can deliver high energy density to satisfy the rapid development of power battery systems. However, conventional solid electrolyte interphase (SEI) or cathode electrolyte interphase (CEI) composed of Li_2CO_3, Li_2O, LiF and alkyl lithium carbonate cannot meet the requirements for high-voltage LMBs in terms of stability and mechanical performance. Herein, a sulfolane-based electrolyte assisted with co-solvent and dual-salt strategies is developed to realize tailored LiF-boride-sulfide-containing interphases on both electrodes, in which the decomposition product RSO_x can combine various inorganic and organic components. The improved integrity of interphases can mitigate the continuous decomposition of the electrolyte, thereby promoting uniform and dense lithium deposition and protecting the structure of cathode materials. Thus, the prepared sulfolane-based electrolyte results in an average Coulombic efficiency of 99.1% for Li||Cu cells and enables 4.7 V Li||$LiNi_{0.8}Co_{0.1}Mn_{0.1}O_2$ cells to maintain 80.0% capacity retention after 200 cycles. Besides, Cu||$LiNi_{0.8}Co_{0.1}Mn_{0.1}O_2$ anode-free cells (3.5 mAh cm^{-2}, capacity retention of 70.5% after 50 cycles) further confirm the practicality of the prepared electrolyte. This work offers a direct and efficient method to enhance the integrity and stability of interphases by optimizing the electrolyte composition.

1. Introduction

To develop next-generation battery technologies to meet the emerging demand for electrochemical energy storage devices with high energy density, lithium metal batteries (LMBs) have received increasing attention due to the intrinsic advantages of lithium metal anode (LMA) in terms of high theoretical specific capacity (3860 mAh g^{-1}) and the lowest electrochemical potential (−3.040 V versus standard hydrogen electrode) [1–3]. Theoretically, the higher energy density can be achieved when LMA is coupled with Ni-rich cathode materials like $LiNi_xCo_yMn_{1-x-y}O_2$ (NCM, x>=0.8) working under an enhanced voltage range (>4.6 V versus Li^+/Li) [2,4].

Unfortunately, the further practical application of such a promising battery system is severely hindered by the instability of the electrode/electrolyte interphases on both cathode and anode sides. Briefly, the unstable electrochemical interphases are mainly derived from the continuously reconfigured solid electrolyte interphase (SEI) accompanying the rampant dendrite growth [5–7], the oxidative decomposition of electrolyte, and the severe destruction of cathode electrolyte interphase (CEI) caused by the uncontrollable reaction between the delithiated cathode and the electrolyte [8–10]. More seriously, these interfacial issues become much more prominent under the harsh but practical battery design like high-loading cathode and limited negative capacity/positive capacity ratio, whereby the cycling stability of LMBs is greatly deteriorated [11–13]. In a fundamental view, the electrolyte plays a vital role in the interfacial behavior, which not only serves as an

* Corresponding authors.
E-mail addresses: dongpeng2001@126.com (P. Dong), yangyang419@xmu.edu.cn (Y. Yang), jbzhao@xmu.edu.cn (J. Zhao).

https://doi.org/10.1016/j.cej.2023.142907
Received 22 December 2022; Received in revised form 24 March 2023; Accepted 8 April 2023
Available online 10 April 2023

ionic link connecting the anode and cathode but also determines the constituent and property of SEI and CEI originating from their decomposition products [14–16]. Therefore, the electrochemical performance of batteries (especially high-voltage LMBs) is closely related to the electrolyte, and it seems to be a direct and efficient way to establish stable electrode/electrolyte interphases through the rational regulation of electrolyte compositions [17–19].

Considering the inevitable and severe oxidative decomposition of the electrolyte at high voltage, the electrolyte system with high anodic stability is preferred to resolve the formidable issues of consistent electrolyte decomposition and to expand the charging potential of NCM cathodes [2,4,20]. However, conventional carbonate-based electrolytes with low intrinsic oxidative stability (commonly ~1 mol L^{-1} (M) lithium hexafluorophosphate ($LiPF_6$) dissolving in a solvent mixture of carbonates) are unable to form stable interphases on the surface of high-voltage cathodes, resulting in poor cycling stability [21,22]. Gases from oxidative decomposition of the carbonate solvent (e.g., CO_2) and decomposition by-products of $LiPF_6$ (e.g., HF) can cause damage to the interphase [23,24], which is required to be suppressed [23,24]. It is not to be neglected that the stability of the interphase depends on its composition. The interphase in carbonate-based electrolytes usually contains components such as Li_2CO_3, Li_2O, LiF and RCO_2Li. Among these, LiF, which can be decomposed by $LiPF_6$, is a common inorganic component with good electrical insulation performance [15,25], and it has been verified that LiF-rich CEI can effectively protect the cathode material from fragmentation [26]. However, its ionic conductivity is low and its flexibility is insufficient. While, it has been reported that the electrolytes consisting of sulfone compounds can form interfacial components with high ionic conductivities of sulfur-containing compounds, thereby effectively reducing the impedance of the interphase and contributing to the formation of the denser and more stable CEI [27,28]. At the same time, sulfone-based electrolytes are promising candidates for high-voltage electrolytes due to their high oxidation resistance, low cost and non-flammability [29–31]. The high valence sulfur in the sulfone functional group is not prone to gas generation due to oxidation [29,32]. Nevertheless, the application of sulfone-based electrolytes has been restricted by their high viscosity and poor compatibility with LMA [33,34]. Obviously, effective and stable interphases require coordination between different components, and how to balance the components needs to be deliberate.

In this work, the stable and robust electrode/electrolyte interphases are constructed in a sulfolane (TMS)-based electrolyte, whereby the reversibility of both LMA and high-voltage cathode is enhanced (Fig. 1). Based on ensuring the anodic stability of TMS, the composition of the electrolyte is modulated by co-solvent (fluoroethylene carbonate, FEC and 1,1,2,2-tetrafluoroethyl-2,2,3,3-tetrafluoropropyl ether, HFE) and dual-salt ($LiPF_6$ and lithium difluoro(oxalate)borate, LiDFOB) strategies. The experiment result suggests that optimized LiF-boride-sulfide-containing interphases are generated, where the sulfur-containing species ensure the ionic conductivity and integrity of the interphases. In such an electrolyte, the reversibility of lithium deposition/stripping is promoted and the growth of lithium dendrites is effectively inhibited. Meanwhile, the electrolyte can mitigate the continuous oxidative decomposition of the electrolyte and protect the structural stability of the cathode material. Therefore, in the designed TMS-based electrolyte, the average Coulombic efficiency (CE) of Li||Cu cells is improved to 99.1%, and long-cycle stability with high CE is achieved for both Li||$LiNi_{0.8}Co_{0.1}Mn_{0.1}O_2$ (NCM811) cells charged to 4.7 V and Li||$LiNi_{0.5}Mn_{1.5}O_4$ (LNMO) cells charged to 4.9 V. Not only that, Cu||NCM811 anode-free cells with the tailored electrolyte are stable for 50 cycles with 70.5% capacity retention, which proves its practicability.

2. Experimental section

2.1. Materials

$LiPF_6$, LiDFOB, FEC and HFE were provided by Zhangjiagang Guotai Huarong New Chemical Materials Co., Ltd. TMS was purchased from Shanghai Aladdin Biochemical Technology Co., Ltd. The cathode materials NCM811 and LNMO were acquired from Beijing Easpring Material Technology Co., Ltd. and Hefei Kejing Material Technology Co., Ltd., respectively. All the chemicals obtained hadn't been further purified.

2.2. Preparation of electrolytes and electrodes

The TMS-based electrolytes were formulated by dissolving 1.2 M $LiPF_6$ in different solvents or solvent blends, including TMS (TMS10), TMS/FEC (9:1 by volume, TF91), TMS/FEC (8:2 by volume, TF82), TMS/FEC (7:3 by volume, TF73), TMS/HFE (8:2 by volume, TH82), TMS/FEC/HFE (8:1:1 by volume, TFH811), TMS/FEC/HFE (7:1:2 by volume, TFH712), TMS/FEC/HFE (6:1:3 by volume, TFH613) and TMS/FEC/HFE (6:2:2 by volume, TFH622), after which were stirred for 3 h (h) at room temperature to mix thoroughly. Here, the maximum volume (vol.) percent of HFE is 30% (Fig. S1). Further, 0.05, 0.1 and 0.15 M LiDFOB were applied to TFH712 to obtain PD-1, PD-2 and PD-3, respectively. The carbonate-based electrolyte (301) was prepared by

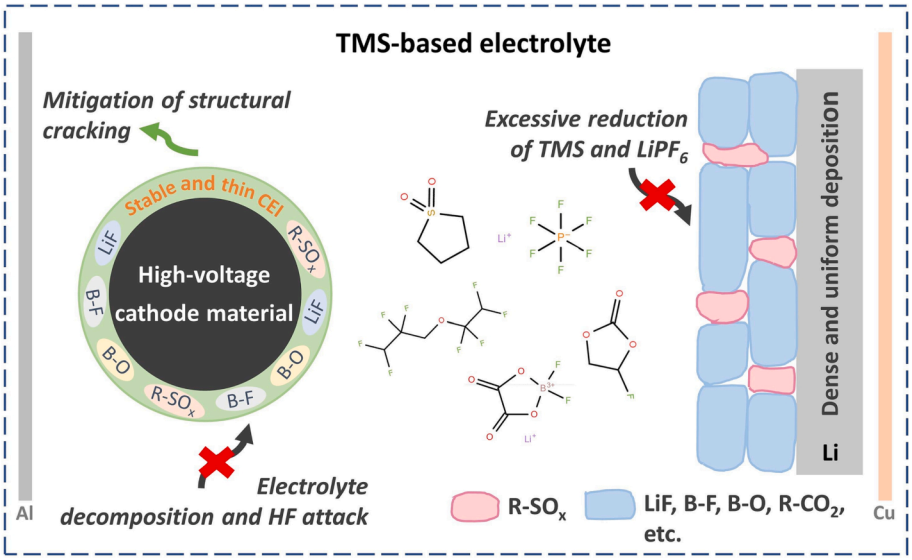

Fig. 1. Schematic illustration of interfacial behaviors in Li||NCM811 charged to 4.7 V using the tailored TMS-based electrolyte.

dissolving 1.2 M $LiPF_6$ in ethylene carbonate/dimethyl carbonate (EC/DMC, 1:1 by mass). 301 + FEC was obtained by adding 10 wt% FEC into 301. All the above were performed in an argon-filled glovebox.

The LNMO (approximately 3.10 mg cm^{-2}, 0.37 mAh cm^{-2}) and NCM811 (approximately 3.27 mg cm^{-2}, 0.68 mAh cm^{-2}) electrodes were fabricated by casting specific slurry on aluminum (Al) foil followed by drying at 80 °C in a vacuum oven overnight. The slurry described was obtained by uniformly dispersing active material, poly-(vinylidene fluoride) and acetylene black (8:1:1 by mass) in a certain amount of n-methyl-2-pyrrolidone solvent. After the electrodes had dried sufficiently, they were punched into small pieces of 12 mm diameter. The high-loading NCM811 electrode is commercial.

2.3. Electrochemical tests

CV tests were operated on a CHI1030C electrochemical workstation (Chenhua, China) for Li||Cu (0–3 V) and Li||NCM811 (3–4.7 V) cells with scan rates of 1 mV s^{-1} and 0.1 mV s^{-1}, respectively. The linear scanning voltammetry (LSV) tests at 3.0–5.5 V were run on a CHI660E electrochemical workstation (Chenhua, China) using Li||Al cells with a sweep speed of 1 mV s^{-1}. In Li||Al cells, lithium sheets were the reference and counter electrode and Al foil was the working electrode. Chronoamperometry (CA) tests were performed for 10 h using CHI660E after charging to 4.7 V (or 4.7/4.8/4.9 V) at 0.1 C in Li||NCM811 (1 C = 200 mA g^{-1}) or Li||LNMO cells (1 C = 120 mA g^{-1}). The EIS of Li||Li and Li||NCM811cells were measured on a Solartron analytical (England) in the frequency range of 0.1–10^5 Hz.

As for Li||Cu cells tests, the method 3 reported by Adama et al. [35] was used to measure the lithium average CE. The test processes were as follows: (1) 5 mAh cm^{-2} lithium was deposited and stripped (to 1 V) on Cu substrate to pretreat; (2) 5 mAh cm^{-2} lithium was deposited (Q_w) on Cu for a working electrode; (3) 1 mAh cm^{-2} lithium was repeatedly stripped (Q_s) and deposited (Q_d) for n cycles (here n = 10); (4) Finally the residual lithium was completely stripped (Q_r) to 1 V. The current density for all the above steps is 0.5 mA cm^{-2}. The average CE is calculated by the following formula:

$$CE = \frac{nQ_S + Q_r}{nQ_d + Q_w} \times 100\% \quad (1)$$

The Li||NCM811 (0.5 C charge and 1 C discharge) and Li||LNMO (1 C charge and discharge) cells equipped with lithium sheets (1 mm thickness) were assembled for testing the long-cycle performance, and they were all cycled at 0.1 C for the first cycle. The Cu||NCM811 anode-free cells were assembled using Cu foils and commercial NCM811 electrodes. The anode-free cell was first activated with 0.1 mA cm^{-2}, subsequently cycling with 0.5 mA cm^{-2} (charging) and 1 mA cm^{-2} (discharging). The Li||Li symmetrical cells were assembled with CR2032 coin-type case, others were with CR2016 coin-type case. 80 μL of electrolyte was added to each case and Asahi Kasei separator was used.

2.4. Characterizations

The ionic conductivity of the electrolytes was measured by a DDS-307A conductivity meter (Leici, China) using a DJS-1C platinum-bright conductivity electrode (Leici, China). The viscosity of the electrolytes was tested with a VM-10A-L viscometer (CBC, Japan). The wettability and contact angle tests (JC-2000C1, POWEREACH, China) were conducted by dropping equal amounts of electrolyte onto the Asahi Kasei separator. The solvation structure of the electrolytes was characterized by Raman spectra, which were carried out by Micro confocal Raman spectrometer (Horiba XploRA, France) with a 532 nm laser. X-ray photoelectron spectroscopy (XPS, Thermo Fisher, America) measurement of the electrodes after 50 cycles was subjected using Escalab Xi^+ test device. As for etching, the time is 0 s, 25 s and 75 s, while the rate is 0.2 nm s^{-1}. The lithium cross-sectional morphology deposited on the Cu substrate and lithium surface morphology after cycling were examined by TM3030 scanning electron microscope (SEM, Hitachi, Japan); whereas the lithium deposition surface morphology and the cycled NCM811 cathodes were observed by Gemini500 (Zeiss, Germany) under SE2 mode. Transmission electron microscopy (TEM) images were gained by JEM2100 equipment (Electronics Co., Ltd., Japan). Atomic force microscope (AFM, Oxford Instruments, China) was used to examine the cycled NCM811 electrodes. All the tested cells were first disassembled in an argon-filled glove box. Afterward, the electrodes were rinsed with pure DMC solvent to remove residual electrolytes and finally dried for subsequent characterization.

3. Results and discussion

Initially, the effect of the co-solvent on the physical properties of the TMS-based electrolytes was investigated by the viscosity and ionic conductivity of the electrolytes at ambient temperature (Fig. S2). Owing to the high viscosity of TMS, the viscosity of TMS10 is as high as 63.6 mPa s. Apparently, the introduction of HFE diminishes the viscosity of the TMS-based electrolytes. Meanwhile, although HFE hardly dissolves the lithium salt, its presence has almost no side effect on the ionic conductivity of the electrolytes, in which TFH613 has a relative increase in conductivity due to the reduction in viscosity. The presence of FEC increases the ionic conductivity of the electrolytes. Not only that, the poor wettability between TMS-based electrolytes and the separator is also solved by the addition of HFE. Even though the concentration of electrolytes is only 1.2 M, neither TMS10 nor TF91 can effectively wet the Asahi Kasei separator (Fig. S3), and the contact angle of TMS10 is quite large (94.4°, Fig. S4). In comparison, due to the low viscosity and low surface tension of HFE, the HFE-containing electrolyte can penetrate the separator easily [34,36]. The incorporation of co-solvent can solve the high viscosity of the TMS-based electrolytes and the poor wettability with the separator.

3.1. Reversibility and characterization of LMA

The compatibility of TMS-based electrolytes with LMA was evaluated by CE tests of Li||Cu cells. As expected, Li||Cu cells with TMS10 exhibit extremely poor stability, which is due to the vigorous side reaction between TMS10 and LMA (Fig. S5a and d) [37]. For comparison, the initial CE (ICE) of Li||Cu cells in TF91 is improved to 96.5%, and the lithium initial nucleation overpotential is reduced from 270.1 mV to 74.1 mV while the deposition/stripping curve becomes stable (Fig. 2b and c, Fig. S5b and e). However, there is a significant increase in voltage polarization. Worse still, micro-short circuits appear during the last stripping (Fig. S5e and S6) [38]. Encouragingly, the average CE of Li||Cu cells exceeds 97.0% in the HFE-containing electrolytes (Fig. 2a), accompanied by flatter polarization voltages without significant increase during cycling (Fig. S7). With the vol.% (HFE) increases, the average CE of Li||Cu cells first increases and then decreases (Fig. 2a). As displayed in Fig. 2a and b, a high average CE of 98.6% is achieved in TFH712, while the initial nucleation overpotential is reduced to 59.2 mV and the ICE is improved to 97.1%. Furthermore, the ratio of FEC is reconfirmed. When vol.% (FEC) increases (in TF82, TF73), the micro-short circuit still occurs (Fig. S8a and b). At the same time, the average CE of Li||Cu cells do not obtain a distinct raise in TFH622 (Fig. S8c), so the vol.% (FEC) of 10% is chosen. It must be mentioned that in TMS-based electrolytes mixed with only FEC (in TF91) or HFE (in TH82), the lithium dendrite growth cannot be well suppressed, as reflected by the severe fluctuations in the voltage–time curves and the micro-short circuit (Fig. S6 and S9). It suggests that the side reactions between TMS-based electrolytes and LMA are better alleviated by the synergistic effect of FEC and HFE, as will be discussed later.

An electrolyte with excellent performance often requires the coordination of multiple components, so the electrode/electrolyte interphases are further optimized to enhance the performance of high-voltage LMBs [23,39]. As shown in Fig. S10, LiDFOB, which can be

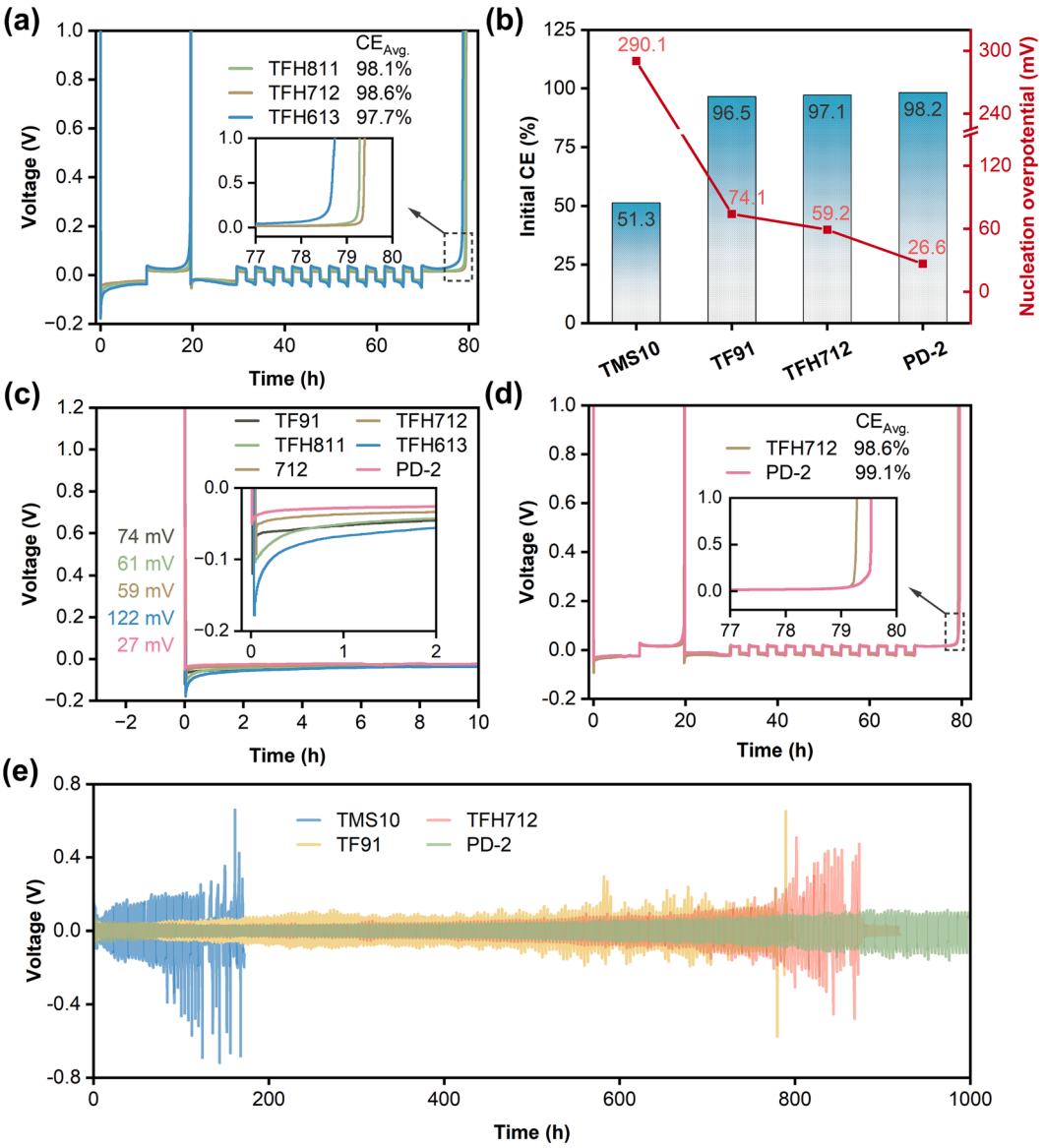

Fig. 2. (a) Voltage-time curves of Li||Cu cells in the electrolytes with different volume percents of HFE, the inset is an enlarged view of the later curve. (b) Comparison of ICE and initial nucleation overpotential. (c) The lithium deposition curves of Li||Cu cells with different electrolytes, where the difference between the lowest point and the stable voltage plateau of the voltage curve is used to calculate the initial nucleation overpotential. The inset is an enlarged view of the initial curve. (d) Voltage-time curves of Li||Cu cells in TFH712 and PD-2. (e) Long-term cycle performances of Li||Li symmetrical cells using different electrolytes at 0.5 mA cm^{-2} and 1 mAh cm^{-2}.

preferentially decomposed at the electrode surface to generate favorable components [40,41], is added to TFH712. The average CE reaches 99.1% in PD-2 and PD-3, which is at a higher level than those reported sulfone-based electrolytes (Table S1). PD-2 is selected due to the higher ICE (98.2%).

Li||Li symmetric cells were also assembled using different electrolytes and then tested for long-term cyclability. The results are displayed in Fig. 2e and Fig. S11. The cells using TMS10 have large polarization voltages (~200 mV) and demonstrate significant voltage fluctuation after 130 h, followed by rapid failure. It illustrates that TMS10 cannot be effective in suppressing interfacial side reactions (Fig. S12a and e). In the electrolytes containing co-solvent, the performance of Li||Li symmetric cells is modified. Meanwhile, the polarization voltage and cycling performance of the cells using TFH712 are better than TF91, which reveals that the lithium deposition/stripping reversibility is better when FEC and HFE coexist. After adding LiDFOB, the cells in PD-2 can cycle steadily for 1000 h and maintain a lower polarization voltage, which indicates that the existence of LiDFOB can promote the formation of a more stable SEI (Fig. S12d and h). The above results are consistent with the performance of Li||Cu cells.

EIS of Li||Li symmetric cells with different electrolytes were carried out to characterize the interfacial resistivity (Fig. S13 and Fig. S14). It is generally considered that the semicircle in the high-frequency region represents the impedance of Li^+ through the SEI (R_{SEI}) [14]. The lowest R_{SEI} of 19.9 Ω is obtained in PD-2, which demonstrates that the presence of LiDFOB can contribute to a higher ionic conductivity SEI and thus enhance lithium deposition/stripping reversibility. Benefiting from the stable SEI, Li||Li symmetric cells using PD-2 exhibit preferable stability and lower polarization voltage even at higher current densities (Fig. S15). Above, the compatibility of TMS-based electrolytes and LMA is effectively improved through the regulation of electrolyte components.

As mentioned in the result above, the compatibility of the TMS-based electrolytes with LMA is enhanced by the synergistic effect of FEC and

HFE. Comparing the CV curves of Li||Cu cells in TMS10 and TF91, the appearance of a new peak in TF91 can be attributed to the formation of SEI, corresponding to the reductive decomposition of FEC (Fig. S16a and b). Therefore, the film-forming effect of FEC on LMA is clear and essential (Fig. S5) [42 43], but the role of HFE needs to be delicately explored. It has been reported that HFE can promote the electrolyte-separator wettability and thus homogeneous the current density of lithium deposition [44–46]. However, the test results display that, although the conductivity and wettability of TFH613 are more dominant (Fig. S2 and Fig. S3), the performance of Li||Cu cells is not optimal, in which both ICE and average CE are relatively degraded (Fig. 2a and Fig. S7). Hence, it is speculated that the role of HFE is not just to improve wettability. Meanwhile, theoretical calculations (Fig. S17) and the Raman spectra result (Fig. S18) suggest that there is no significant difference in the coordination environment of Li^+ in different electrolytes, thus ruling out the effect of the change of the solvation structure on the performance of LMA.

On the other hand, the effect of HFE on the initial nucleation overpotential is of interest. From the EIS results, the presence of HFE can significantly reduce the charge transfer impedance, and thus the nucleation overpotential is reduced (Fig. S13) [47]. The morphology of lithium deposition in electrolytes with different vol.% (HFE) is contrasted. The optical photograph (Fig. 3a) shows that the deposited lithium with TF91 is uneven distribution and part of the Cu foil is exposed, which reveals a spotty deposition morphology. By contrast, when HFE is mixed in, a uniformly distributed deposited lithium is formed, almost covering the Cu foil (Fig. 3b, Fig. S19b and c). According to the classical nucleation theory, the particle size of deposited lithium is inversely proportional to the overpotential, and the morphology of initially deposited lithium is conducive to the subsequent deposition process [48,49]. Thus, the SEM images of the deposited lithium were compared. The HFE-containing TMS-based electrolytes result in more dense and uniform deposited lithium in comparison with TF91 (Fig. 3d and e, Fig. S19e and f). Meanwhile, relatively large particles are obtained using TFH712 (with an initial nucleation overpotential of 59.2 mV). However, as the vol.% (HFE) continues to increase, the initial nucleation overpotential increases to 122.1 mV (TFH613, Fig. 2c). At the same time, the deposited lithium particles become smaller and less dense but are still uniformly distributed (Fig. S19f). From this, it's concluded that an appropriate proportion of HFE can reduce the initial nucleation overpotential, thereby synergizing with FEC for regulating the lithium deposition process and hindering the vigorous reaction of TMS with LMA.

While compared with TFH712, larger and denser deposited lithium is obtained in PD-2 with a thickness of only 26 μm (Fig. 3f and i). The deposited lithium in this form can dramatically reduce the reactive surface area and inhibit the formation of dendritic lithium, thereby significantly improving the cycling stability of lithium deposition/stripping.

Necessarily, the composition of SEI in different electrolytes was characterized by XPS tests (Fig. 4). As shown in the C 1s and O 1s spectra, C-C/C-H (284.8 eV, C 1s), C-O (286.6 eV, C 1s and 530.8 eV, O 1s), C═O (288.2 eV, C 1 s), O-C═O (533 eV, O 1s) species mainly produced by solvent decomposition are detected, and these organic components can cope with the volume change of SEI during cycling but have poor mechanical properties. As for the F 1s spectrum, the inorganic component LiF (684.9 eV, F 1s) is present in the SEI films of all electrolytes, which is derived from the decomposition of $LiPF_6$ or FEC. LiF has good electronic insulation and mechanical properties and has been shown to inhibit lithium dendrite growth, but its ionic conductivity is insufficient. In addition, the decomposition products of $LiPF_6$ can react with traces of water to produce the harmful gas HF [24,50]. The S 2p spectrum shows that all electrolytes contain sulfur-containing species such as RSO_3 (168.6 eV, 169.7 eV) and RSO_2 (166.5 eV, 167.7 eV), which are generated by TMS decomposition and have high ionic conductivity [51,52] (Fig. 4d). However, it is not negligible that excessive

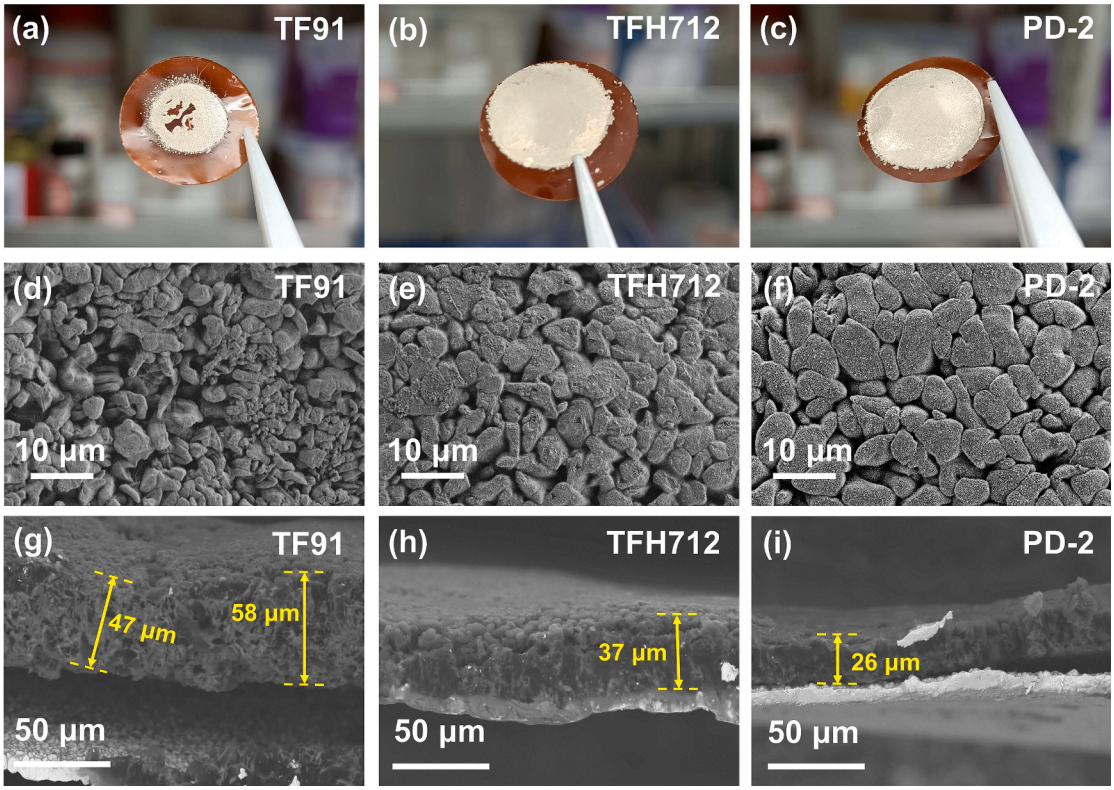

Fig. 3. Optical and top-view SEM images of deposited lithium on Cu substrate in Li||Cu cells using different electrolytes, at a current density of 0.5 mA cm^2 with a deposition capacity of 5 mAh cm^2 lithium: (a, d) TF91, (b, e) TFH712 and (c, f) PD-2. The cross-sectional SEM images of deposited lithium of (g) TF91, (h) TFH712 and (i) PD-2.

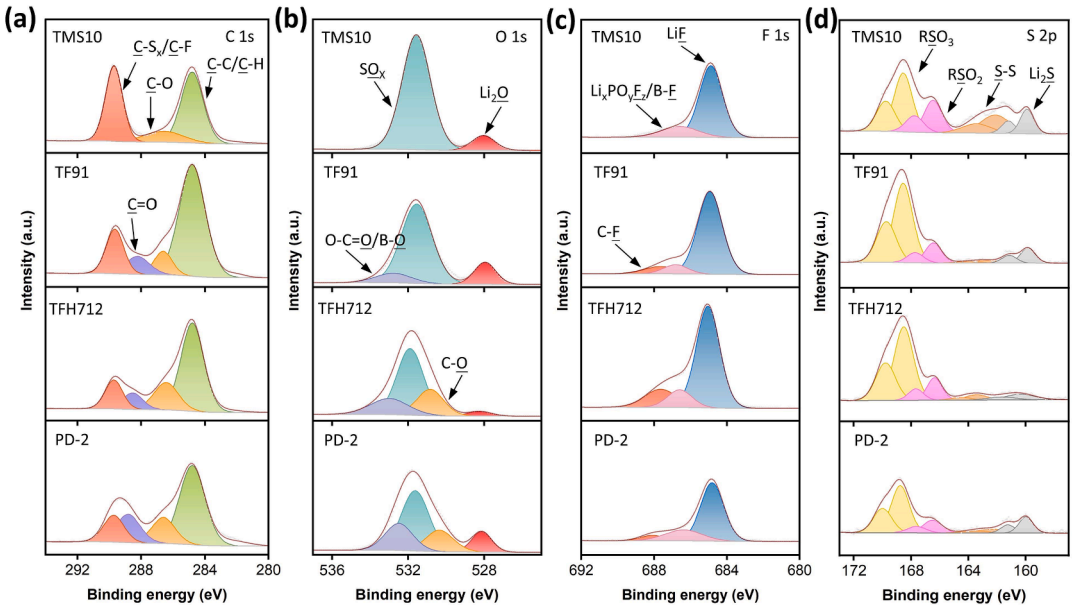

Fig. 4. XPS characterization test results of the LMA surface after 50 cycles in Li||NCM811 cells with different electrolytes: (a) C 1s, (b) O 1s, (c) F 1s and (d) S 2p spectra.

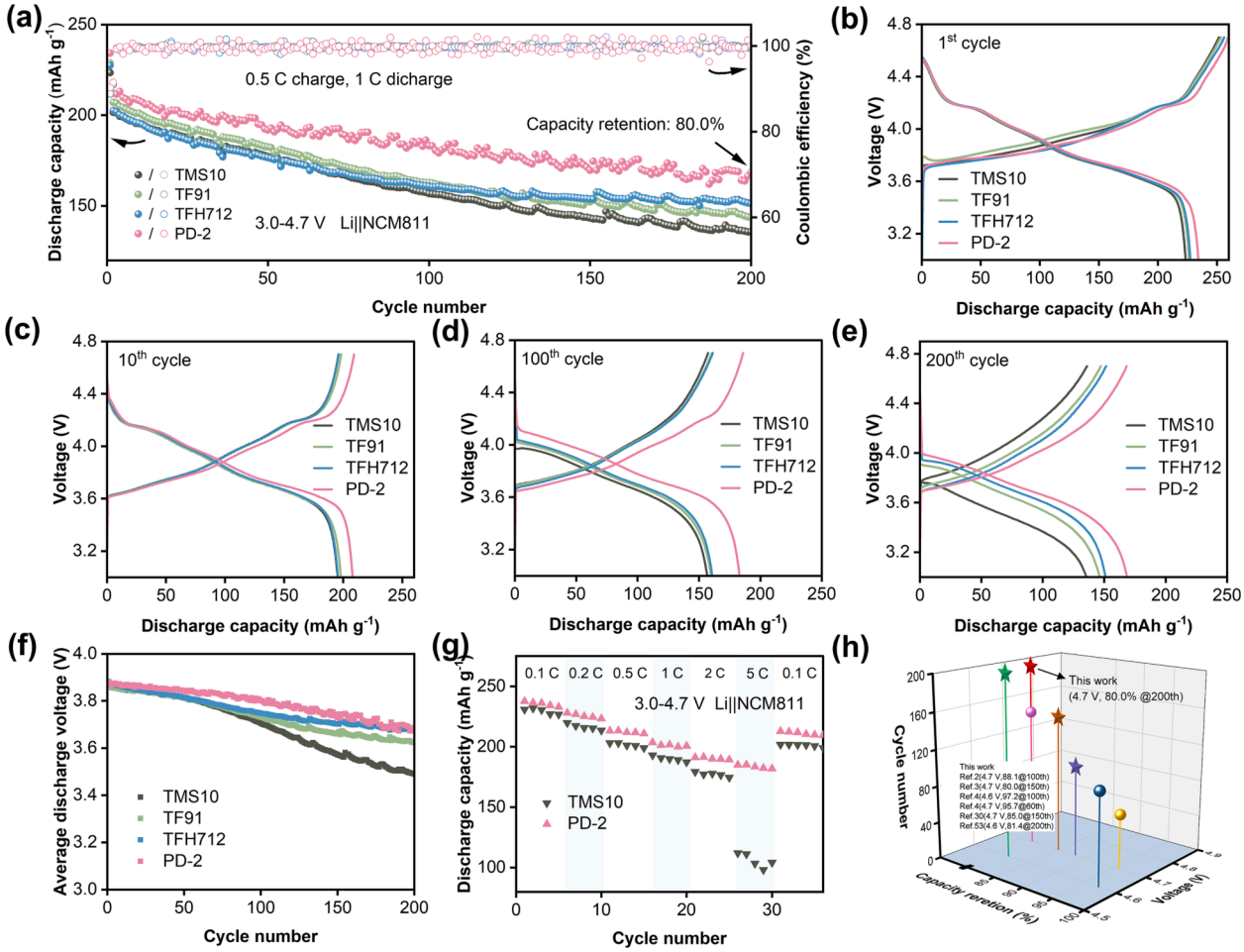

Fig. 5. Electrochemical performance of Li||NCM811 cells at a charge cut-off voltage of 4.7 V using different electrolytes. (a) Long-cycle performance. (b) Initial charge–discharge curves at 0.1 C (1 C = 200 mA g^{-1}). The charge and discharge curves at the cycle of (c) 10th, (d) 100th and (e) 200th. (f) Average discharge voltage during cycling. (g) Rate performance test of TMS10 and PD-2. (h) Comparison of the long-cycle performance of this work with others reported work [2–4,30,54]. The spherical icon refers to the single-crystalline material used in the literature, and the rest is the poly-crystalline material.

decomposition of the electrolyte components is detrimental to the stability of SEI. In the presence of LiDFOB, the intensity of LiF and sulfur-containing compounds peaks is significantly reduced, which indicates that the decomposition of $LiPF_6$ and TMS greatly suppressed in PD-2. The attenuated $Li_xPO_yF_y$ peak also proves the reduction of $LiPF_6$ decomposition (686.6 eV, F 1s; 133.4 eV; P 2p in Fig. S20). Meanwhile, favorable B-containing components such as B-F (194.0 eV, B 1s) and B-O (192.6 eV, B 1s) are generated (Fig. S16d and S21), which can induce denser lithium deposition to reduce the reactive area. Notably, the decomposition of LiDFOB can contribute a certain amount of LiF, but the intensity of LiF species peak is significantly reduced due to the inhibition of $LiPF_6$ decomposition [53]. In short, through the modulation of electrolyte components, LiF-boride-sulfide-containing SEI is constructed in PD-2 to reduce excessive electrolyte decomposition and promote dense and uniform lithium deposition, thereby effectively improving the reversibility of LMA.

3.2. Electrochemical performance and characterization of high-voltage LMBs

According to the results of the LSV test, the oxidation potential of these TMS-based electrolytes all exceed 5.0 V, demonstrating their promising oxidation resistance (Fig. S22). To investigate their stability in high-voltage LMBs, Li||NCM811 cells at a charge cut-off voltage of 4.7 V were tested. It can be seen that PD-2 has a lower static leakage current than the others, which indicates that a more stable CEI layer can be formed in it, thereby slowing down the parasitic reaction (Fig. S23). Before cycling, CV tests using different electrolytes were performed to investigate the cathode stability in Li||NCM811 cells (Fig. S24). The redox peak patterns of these four electrolytes were similar in the first cycle. And all electrolytes exhibit three pairs of redox peaks, which structurally represent the phase transition process of H1-M−H2−H3 [54].

The long-cycling test results are shown in Fig. 5a-f. During the first cycle at 0.1 C, Li||NCM811 cells using TMS10, TF91, TFH712 and PD-2 exhibit similar initial lithiation/delithiation curves with ICEs of 88.8%, 88.9%, 89.4% and 90.3%, respectively, in which the highest discharge specific capacity of 234.1 mAh g^{-1} is released in PD-2. As shown in Fig. 5a, Li||NCM811 cells with PD-2 exhibit good stability, which have a first discharge specific capacity of 212.0 mAh g^{-1} at 1 C, and the capacity retention of the cells after 200 cycles is 80.0% with a high average CE of 99.7%. In contrast, Li||NCM811 cells using TMS10, TF91 and TFH712 present relatively poor cycling stability, with capacity retentions of 67.3%, 71.8% and 74.6% after 200 cycles, respectively. Even so, the high-voltage cycle stability of TMS-based electrolytes is still better than that of carbonate-based electrolytes (Fig. S25). Not only that, Li||NCM811 cells in PD-2 can maintain a higher and more stable average discharge voltage during cycling (Fig. 5f), and exhibit an excellent rate performance releasing a discharge specific capacity of 184.8 mAh g^{-1} (77.8% of 0.1 C) at 5 C (Fig. 5g). Specifically, the TMS-based electrolyte optimized in this work demonstrates good long-cycle performance in high-voltage LMBs (charging voltage >4.5 V versus Li^+/Li) compared to other reported works (Fig. 5h).

The high-voltage performance of TMS-based electrolytes was also tested in 4.9 V Li||LNMO cells (Fig. S26-S30). Compared with TF91, Li||LNMO cells using TFH712 and PD-2 have better cycling stability, with 80.1% and 98.0% capacity retention after 500 cycles, respectively. Not only that, the discharge specific capacity of PD-2 can still maintain 90.0% of the highest discharge specific capacity after 700 cycles, showing excellent high-voltage and long-cycle stability (Fig. S29). Notably, Li||LNMO cells in TMS10 exhibit severe overcharge with a low CE, which is inconsistent with its high electrochemical oxidation resistance (Fig. S28a and S30). From the CA test of Li||LNMO cells, it's suggested that the reason may be that the CEI formed in TMS10 cannot effectively solve the interfacial instability problem at higher voltage (Fig. S31) [55]. Thus, although the four electrolytes have comparable oxidation resistance, their electrochemical stability in the high-voltage LMBs system differs considerably, which is closely related to the properties of the electrode/electrolyte interphases.

Therefore, to deeply understand the performance difference of different electrolytes on high-voltage LMBs, TEM, XPS, SEM and AFM tests were used to investigate the NCM811 cathodes after 50 cycles. Compared with the other electrolytes, thin (≈ 4.5 nm) and uniform CEI is obtained in PD-2, indicating less destruction/reconstruction of CEI during cycling, which can protect the cathode well (Fig. 6a-d). According to the XPS results of different sputtering times, the CEI generated by PD-2 has sulfur-containing species with high ionic conductivity [56,57] (Fig. S32), along with LiF (685.7 eV, F 1 s), B-F (193.7 eV, B 1 s) and B-O (191.3 eV, B 1 s) species (Fig. 6e-g). At the same time, the peak intensities of LiF and Li_xPF_y (689.2 eV, F 1 s) are reduced in PD-2 compared with TFH712, suggesting that the addition of LiDFOB inhibits the decomposition of $LiPF_6$ and consequently mitigates the HF attack (Fig. S33c) [50,58].

The elastic modulus of CEI films after cycling in the different electrolytes was measured using AFM (Fig. S34). Compared to carbonate-based electrolytes the CEI film in TMS-based electrolytes (TFH712 and PD-2) has a more uniform and high elastic modulus, which indicates its higher mechanical strength. Although the interphase of 301 + FEC and TFH712 contains organic and inorganic components such as LiF, Li_2O and RCO_2Li [50] (Fig. S33), the mechanical strength of the CEI film increases due to the presence of RSO_x in TFH712. In other words, RSO_x may be able to tightly combine the organic and inorganic components, thus improving the integrity and mechanical strength of the interphases. Meanwhile, the addition of LiDFOB can introduce B-containing species that contribute to the mechanical strength of CEI films.

Summarily, a robust and uniform CEI can be formed in PD-2 by adjusting the electrolyte composition, thereby reducing the excess decomposition of the electrolyte, effectively protecting the structure of the cathode material under high-voltage (Fig. 6h and i), and improving the long-cycle performance.

Considering the favorable compatibility of PD-2 with LMA and high-voltage cathode (Fig. 7a), Cu||NCM811 anode-free cells were investigated at a charge cut-off voltage of 4.7 V. Under such harsh conditions, the cycling stability is greatly limited by the reversibility of the lithium deposition/stripping and side reactions at the electrode/electrolyte interphases [12,13,59]. 301 + FEC is chosen as the comparison sample, which can generate LiF-rich but RSO_x-free interphases (Fig. S35). The results are shown in Fig. 7b-d and Fig. S36. In 301 + FEC, the capacity of the cells decays with low CE as the voltage polarization increases, probably due to the rapid consumption of active lithium during cycling. Compared with the carbonate-based electrolyte without RSO_x, the performance of Cu||NCM811 cells in THF712 and PD-2 is advantageous (Fig. S36). And the performance of anode-free cells in PD-2 is significantly improved with a capacity retention of 70.5% after 50 cycles and a lithium consumption of only 0.7% per cycle (Fig. 7b and c). These results demonstrate the potential of PD-2 for high-energy–density battery system applications.

4. Conclusion

In summary, high-voltage LMBs with excellent performance have been realized by a TMS-based electrolyte. The LiF-boride-sulfide-containing electrode/electrolyte interphases are constructed via electrolyte components regulation, in which RSO_x can combine various inorganic and organic components to enhance the mechanical strength of interphases. Taking advantage of the synergistic effects of FEC and HFE, the reversibility of lithium deposition/stripping is significantly enhanced, while the excessive decomposition of $LiPF_6$ is suppressed by LiDFOB. As a result, the growth of lithium dendrites is restrained due to the stable SEI and the lithium average CE is improved to 99.1%. Meanwhile, the continuous side reaction between the electrolyte and the cathode is inhibited by the uniform and robust CEI, thus enabling the

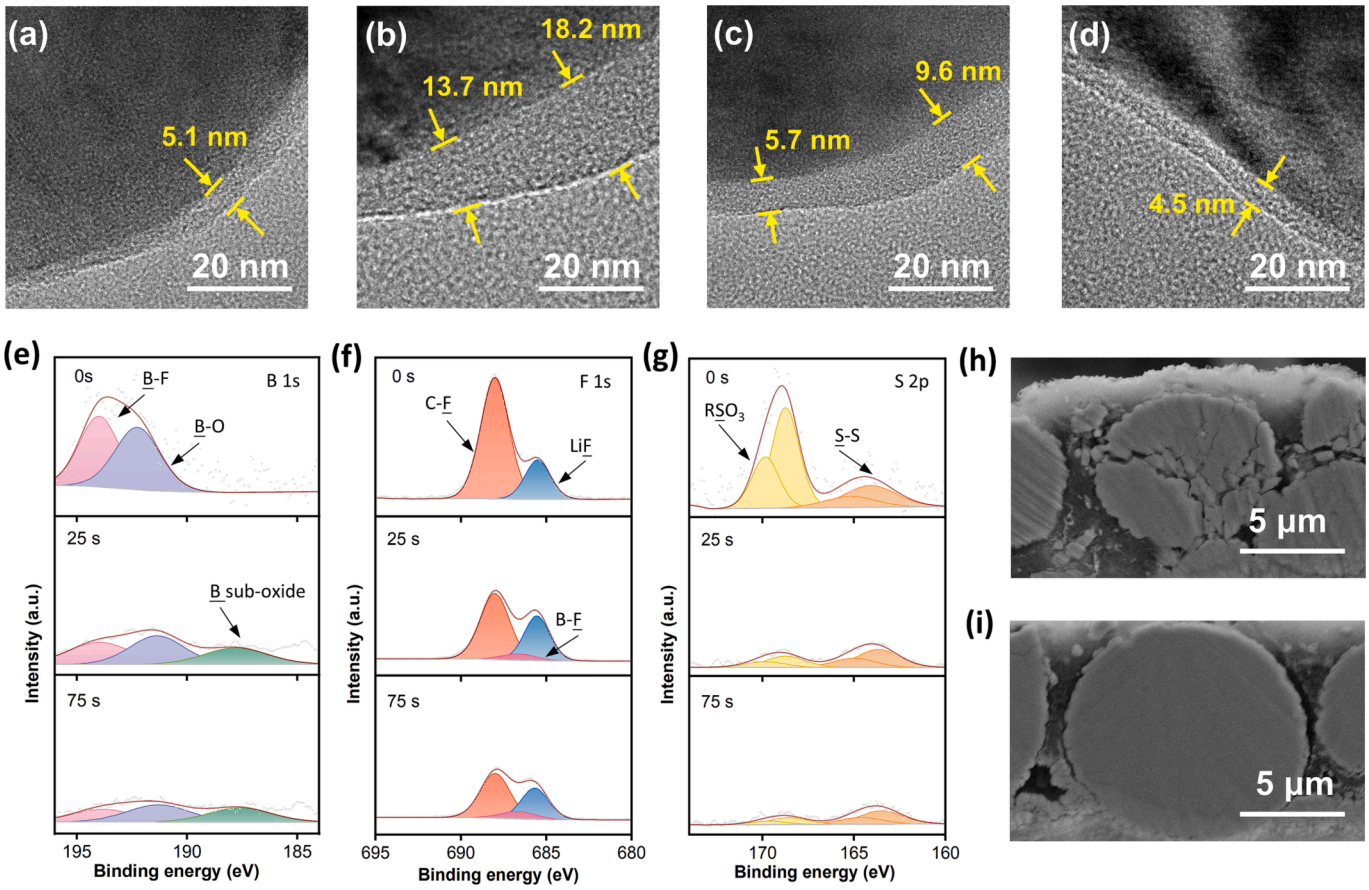

Fig. 6. Characterization of NCM811 after cycling in different electrolytes. TEM images using (a) TMS10, (b) TF91, (c) TFH712 and (d) PD-2. The XPS analysis of different sputtering times using PD-2: (e) B 1s, (f) F 1s and (g) S 2p spectra. Cross-sectional SEM images of (h) TMS10 and (i) PD-2.

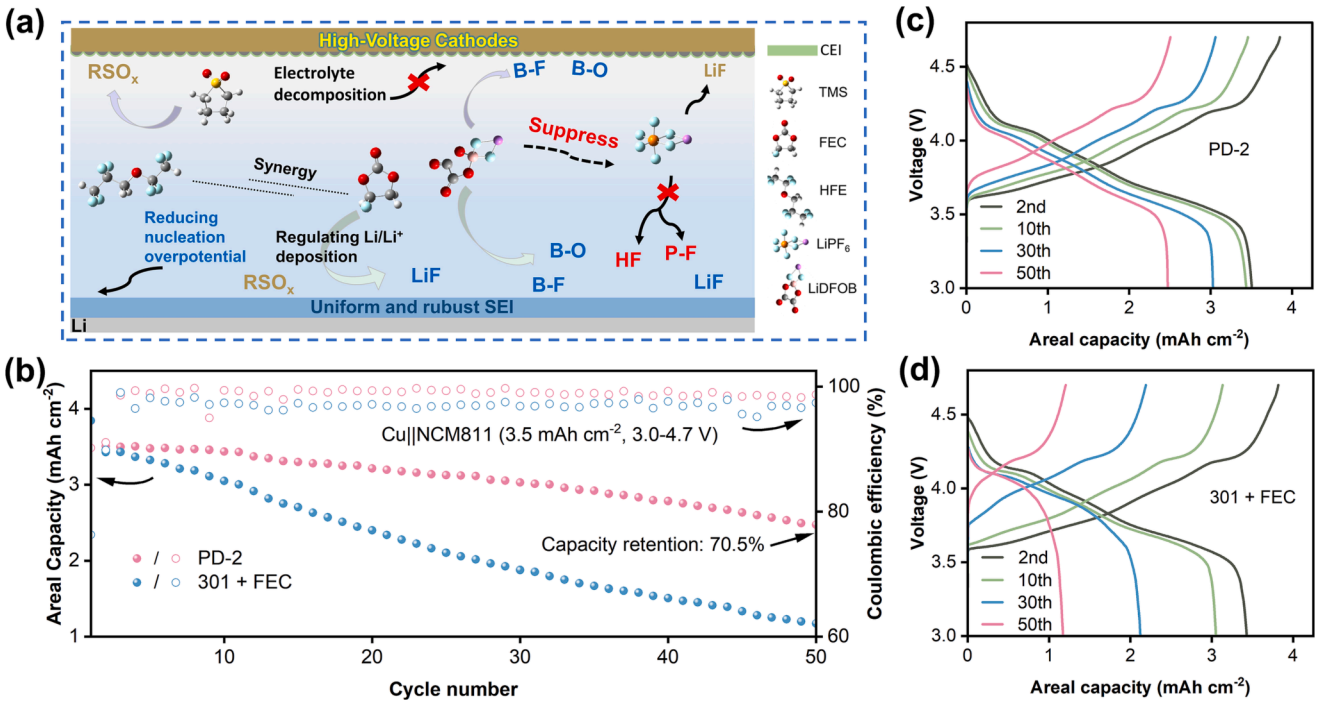

Fig. 7. (a) Schematic diagram of PD-2 in high-voltage LMBs. (b) The cycling performance in Cu||NCM811 anode-free cells using PD-2 and 301 + FEC. The charge and discharge curves at different cycles of (c) PD-2 and (d) 301 + FEC.

stable cycling of high-voltage LMBs. In addition, a Li loss rate of only 0.7% for each cycle is achieved in Cu||NCM811 anode-free cells under harsh but practical conditions. This work provides an economical and attractive way to design functional electrolytes for high-voltage LMBs and a reference for exploring the role of fluorinated ether solvents for LMA.

Declaration of Competing Interest

The authors declare that they have no known competing financial interests or personal relationships that could have appeared to influence the work reported in this paper.

Data availability

The authors do not have permission to share data.

Acknowledgments

We gratefully acknowledge the financial support of National Key Research and Development Program of China (2021YFB2400300), National Natural Science Foundation of China (21875198 and 22109030), the Key Project of Science and Technology of Xiamen (3502Z20201013), the Key Research and Development Program of Yunnan Province (202103AA080019), Fujian Industrial Technology Development and Application Plan (2022I0002) and Guangdong Basic and Applied Basic Research Foundation (2021A1515010177). We would like to express gratitude to Tan Kah Kee Innovation Laboratory (IKKEM) for help with XPS and SEM. In terms of DFT calculation and MD simulation, we were appreciative to Beijing PARATERA Tech CO., Ltd. for HPC resources (URL: https://paratera.com/).

Appendix A. Supplementary data

Supplementary data to this article can be found online at https://doi.org/10.1016/j.cej.2023.142907.

References

[1] M.S. Kim, Z. Zhang, P.E. Rudnicki, Z. Yu, J. Wang, H. Wang, S.T. Oyakhire, Y. Chen, S.C. Kim, W. Zhang, D.T. Boyle, X. Kong, R. Xu, Z. Huang, W. Huang, S. F. Bent, L.W. Wang, J. Qin, Z. Bao, Y. Cui, Suspension electrolyte with modified Li(+) solvation environment for lithium metal batteries, Nat. Mater. 21 (4) (2022) 445–454, https://doi.org/10.1038/s41563-021-01172-3.

[2] W. Xue, M. Huang, Y. Li, Y.G. Zhu, R. Gao, X. Xiao, W. Zhang, S. Li, G. Xu, Y. Yu, P. Li, J. Lopez, D. Yu, Y. Dong, W. Fan, Z. Shi, R. Xiong, C.-J. Sun, I. Hwang, W.-K. Lee, Y. Shao-Horn, J.A. Johnson, J. Li, Ultra-high-voltage Ni-rich layered cathodes in practical Li metal batteries enabled by a sulfonamide-based electrolyte, Nat. Energy 6 (5) (2021) 495–505, https://doi.org/10.1038/s41560-021-00792-y.

[3] F. Liu, Z. Zhang, Z. Yu, X. Fan, M. Yi, M. Bai, Y. Song, Q. Mao, B.o. Hong, Z. Zhang, Y. Lai, Bifunctional nitrile-borate based electrolyte additive enables excellent electrochemical stability of lithium metal batteries with single-crystal Ni-rich cathode at 4.7 V, Chem. Eng. J. 434 (2022) 134745.

[4] L. Tan, S. Chen, Y. Chen, J. Fan, D. Ruan, Q. Nian, L. Chen, S. Jiao, X. Ren, Intrinsic nonflammable ether electrolytes for ultrahigh-voltage lithium metal batteries enabled by chlorine functionality, Angew. Chem.-Int. Edit. 61 (32) (2022) e202203693.

[5] S. Li, Q. Liu, W. Zhang, L. Fan, X. Wang, X. Wang, Z. Shen, X. Zang, Y. Zhao, F. Ma, Y. Lu, High-efficacy and polymeric solid-electrolyte interphase for closely packed Li electrodeposition, Adv. Sci. 8 (6) (2021) 2003240, https://doi.org/10.1002/advs.202003240.

[6] P. Li, L. Chen, Z. Wen, D. Zhang, Y. Zhang, N. Zhang, G. Chen, X. Liu, Solvation chemistry of rare earth nitrates in carbonate electrolyte for advanced lithium metal batteries, Chem. Eng. J. 433 (2022) 134468.

[7] Y. Fan, X. He, H. Li, Y. Huang, C. Sun, H. Liu, E. Huangzhang, F. Sun, X. Zhao, J. Nan, Lithiophilic Ni3S2 layer decorated nickel foam (Ni3S2@Ni foam) with fast ion transfer kinetics for long-life lithium metal anodes, Chem. Eng. J. 450 (2022) 138384.

[8] P. Bai, X. Ji, J. Zhang, W. Zhang, S. Hou, H. Su, M. Li, T. Deng, L. Cao, S. Liu, X. He, Y. Xu, C. Wang, Formation of LiF-rich Cathode-Electrolyte Interphase by Electrolyte Reduction, Angew. Chem.-Int. Edit. 61 (26) (2022) e202202731, https://doi.org/10.1002/anie.202202731.

[9] W. Liu, J. Li, W. Li, H. Xu, C. Zhang, X. Qiu, Inhibition of transition metals dissolution in cobalt-free cathode with ultrathin robust interphase in concentrated electrolyte, Nat. Commun. 11 (1) (2020) 3629, https://doi.org/10.1038/s41467-020-17396-x.

[10] J. Wang, S. Guo, X. Wang, L. Gu, D. Su, Structural degradation of Ni-rich layered oxide cathode for Li-ion batteries, J. Electrochem. 28 (2) (2022) 77–100, https://doi.org/10.13208/j.electrochem.210843.

[11] X. Ren, L. Zou, X. Cao, M.H. Engelhard, W. Liu, S.D. Burton, H. Lee, C. Niu, B. E. Matthews, Z. Zhu, C. Wang, B.W. Arey, J. Xiao, J. Liu, J.-G. Zhang, W. Xu, Enabling high-voltage lithium-metal batteries under practical conditions, Joule 3 (7) (2019) 1662–1676, https://doi.org/10.1016/j.joule.2019.05.006.

[12] F. Qiu, X. Li, H. Deng, D. Wang, X. Mu, P. He, H. Zhou, A concentrated ternary-salts electrolyte for high reversible Li metal battery with slight excess Li, Adv. Energy Mater. 9 (6) (2018) 1803372, https://doi.org/10.1002/aenm.201803372.

[13] T.D. Pham, A. Bin Faheem, J. Kim, H.M. Oh, K.K. Lee, Practical high-voltage lithium metal batteries enabled by tuning the solvation structure in weakly solvating electrolyte, Small 18 (14) (2022) e2107492.

[14] N. Piao, S. Liu, B. Zhang, X. Ji, X. Fan, L. Wang, P.-F. Wang, T. Jin, S.-C. Liou, H. Yang, J. Jiang, K. Xu, M.A. Schroeder, X. He, C. Wang, Lithium metal batteries enabled by synergetic additives in commercial carbonate electrolytes, ACS Energy Lett. 6 (5) (2021) 1839–1848, https://doi.org/10.1021/acsenergylett.1c00365.

[15] D. Wu, J. He, J. Liu, M. Wu, S. Qi, H. Wang, J. Huang, F. Li, D. Tang, J. Ma, Li2CO3 /LiF-rich heterostructured solid electrolyte interphase with superior lithiophilic and Li+-transferred characteristics via adjusting electrolyte additives, Adv. Energy Mater. 12 (18) (2022) 2200337, https://doi.org/10.1002/aenm.202200337.

[16] J. Li, H. Hua, X. Deng, P. Lai, Y. Kang, S. Kuang, F. Wang, X. Zeng, Y. Zhang, J. Zhao, Mild and controllable solid electrolyte interphase formation for high-voltage lithium metal batteries in a wide-temperature range from −40 °C to 80 °C, Chem. Eng. J. 452 (2023) 139398.

[17] R. Wang, X. Dai, Z. Qian, Y. Sun, S. Fan, K. Xiong, H. Zhang, F. Wu, In situ surface protection for enhancing stability and performance of LiNi0.5Mn0.3Co0.2O2 at 4.8 V: the working mechanisms, ACS Mater. Lett. 2 (4) (2020) 280–290, https://doi.org/10.1021/acsmaterialslett.9b00476.

[18] X. Fan, L. Chen, O. Borodin, X. Ji, J. Chen, S. Hou, T. Deng, J. Zheng, C. Yang, S. C. Liou, K. Amine, K. Xu, C. Wang, Non-flammable electrolyte enables Li-metal batteries with aggressive cathode chemistries, Nat. Nanotechnol. 13 (8) (2018) 715–722, https://doi.org/10.1038/s41565-018-0183-2.

[19] L. Li, G. Xu, S. Zhang, S. Dong, S. Wang, Z. Cui, X. Du, C. Wang, B. Xie, J. Du, X. Zhou, G. Cui, Highly fluorinated Al-centered lithium salt boosting the interfacial compatibility of Li-metal batteries, ACS Energy Lett. 7 (2) (2022) 591–598, https://doi.org/10.1021/acsenergylett.1c02489.

[20] Z. Wang, H. Zhang, J. Xu, A. Pan, F. Zhang, L. Wang, R. Han, J. Hu, M. Liu, X. Wu, Advanced ultralow-concentration electrolyte for wide-temperature and high-voltage Li-metal batteries, Adv. Funct. Mater. 32 (23) (2022) 2112598.

[21] Z. Piao, R. Gao, Y. Liu, G. Zhou, H.M. Cheng, A review on regulating Li(+) solvation structures in carbonate electrolytes for lithium metal batteries, Adv. Mater. (2022) e2206009.

[22] Q. Ma, X. Zhang, A. Wang, Y. Xia, X. Liu, J. Luo, Stabilizing solid electrolyte interphases on both anode and cathode for high areal capacity, high-voltage lithium metal batteries with high Li utilization and lean electrolyte, Adv. Funct. Mater. 30 (32) (2020) 2002824.

[23] R. Pan, Z. Cui, M. Yi, Q. Xie, A. Manthiram, Ethylene carbonate-free electrolytes for stable, safer high-nickel lithium-ion batteries, Adv. Energy Mater. 12 (19) (2022) 2103806, https://doi.org/10.1002/aenm.202103806.

[24] J.G. Han, K. Kim, Y. Lee, N.S. Choi, Scavenging materials to stabilize LiPF6 -containing carbonate-based electrolytes for Li-ion batteries, Adv. Mater. 31 (20) (2019) e1804822.

[25] X.Z. Xiaodi Ren, Z. Shadike, L. Zou, Designing advanced in situ electrode-electrolyte interphases for wide temperature operation of 4.5 V Li-LiCoO2 batteries, Adv. Mater. 24 (11) (2020) 8, https://doi.org/10.1002/adma.202004898.

[26] X. Ren, P. Gao, L. Zou, S. Jiao, X. Cao, X. Zhang, H. Jia, M.H. Engelhard, B. E. Matthews, H. Wu, H. Lee, C. Niu, C. Wang, B.W. Arey, J. Xiao, J. Liu, J.G. Zhang, W. Xu, Role of inner solvation sheath within salt-solvent complexes in tailoring electrode/electrolyte interphases for lithium metal batteries, Proc. Natl. Acad. Sci. U.S.A. 117 (46) (2020) 28603–28613, https://doi.org/10.1073/pnas.2010852117.

[27] H. Cai, H. Jing, X. Zhang, M. Shen, Q. Wang, Improving high-voltage performance of lithium-ion batteries with sulfolane as an electrolyte additive, J. Electrochem. Soc. 164(4) (2017) A714-A720. doi: 10.1149/2.0801704jes.

[28] S. Li, X. Xu, X. Shi, B. Li, Y. Zhao, H. Zhang, Y. Li, W. Zhao, X. Cui, L. Mao, Composition analysis of the solid electrolyte interphase film on carbon electrode of lithium-ion battery based on lithium difluoro(oxalate)borate and sulfolane, J. Power Sources 217 (2012) 503–508, https://doi.org/10.1016/j.jpowsour.2012.05.114.

[29] J. Alvarado, M.A. Schroeder, M. Zhang, O. Borodin, E. Gobrogge, M. Olguin, M. S. Ding, M. Gobet, S. Greenbaum, Y.S. Meng, K. Xu, A carbonate-free, sulfone-based electrolyte for high-voltage Li-ion batteries, Mater. Today 21 (4) (2018) 341–353, https://doi.org/10.1016/j.mattod.2018.02.005.

[30] W. Hou, D. Zhu, S. Ma, W. Yang, H. Yan, Y. Dai, High-voltage nickel-rich layered cathodes in lithium metal batteries enabled by a sulfolane / fluorinated ether/fluoroethylene carbonate-based electrolyte design, J. Power Sources 517 (2022) 230683.

[31] L. Dong, Y. Liu, D. Chen, Y. Han, Y. Ji, J. Liu, B. Yuan, Y. Dong, Q. Li, S. Zhou, S. Zhong, Y. Liang, M. Yang, C. Yang, W. He, Stabilization of high-voltage lithium metal batteries using a sulfone-based electrolyte with bi-electrode affinity and LiSO2F-rich interphases, Energy Storage Mater. 44 (2022) 527–536, https://doi.org/10.1016/j.ensm.2021.10.045.

[32] L. Xing, W. Tu, J. Vatamanu, Q. Liu, W. Huang, Y. Wang, H. Zhou, R. Zeng, W. Li, On anodic stability and decomposition mechanism of sulfolane in high-voltage lithium ion battery, Electrochim. Acta 133 (2014) 117–122, https://doi.org/10.1016/j.electacta.2014.03.190.
[33] W. Wu, Y. Bai, X. Wang, C. Wu, Sulfone-based high-voltage electrolytes for high energy density rechargeable lithium batteries: progress and perspective, Chin. Chem. Lett. 32 (4) (2020) 1309–1315, https://doi.org/10.1016/j.cclet.2020.10.009.
[34] X. Ren, S. Chen, H. Lee, D. Mei, M.H. Engelhard, S.D. Burton, W. Zhao, J. Zheng, Q. Li, M.S. Ding, M. Schroeder, J. Alvarado, K. Xu, Y.S. Meng, J. Liu, J.-G. Zhang, W. Xu, Localized High-concentration sulfone electrolytes for high-efficiency lithium-metal batteries, chem 4 (8) (2018) 1877–1892, https://doi.org/10.1016/j.chempr.2018.05.002.
[35] B.D. Adams, J. Zheng, X. Ren, W. Xu, J.G. Zhang, Accurate determination of coulombic efficiency for lithium metal anodes and lithium metal batteries, Adv. Energy Mater. 8 (7) (2017) 1702097, https://doi.org/10.1002/aenm.201702097.
[36] H. Zheng, X. Zhou, S. Cheng, R. Xia, S. Nie, X. Liang, Y. Sun, H. Xiang, High-voltage LiNi0.5Mn1.5O4 cathode stability of fluorinated ether based on enhanced separator wettability, J. Electrochem. Soc. 166(8) (2019) A1456-A1462. doi: 10.1149/2.0601908jes.
[37] S. Lin, H. Hua, P. Lai, J. Zhao, A multifunctional dual-salt localized high-concentration electrolyte for fast dynamic high-voltage lithium battery in wide temperature range, Adv. Energy Mater. 11 (36) (2021) 2101775, https://doi.org/10.1002/aenm.202101775.
[38] Y. Zhao, T. Zhou, T. Ashirov, M.E. Kazzi, C. Cancellieri, L.P.H. Jeurgens, J.W. Choi, A. Coskun, Fluorinated ether electrolyte with controlled solvation structure for high voltage lithium metal batteries, Nat. Commun. 13 (1) (2022) 2575, https://doi.org/10.1038/s41467-022-29199-3.
[39] J. Zhao, Y. Liang, X. Zhang, Z. Zhang, E. Wang, S. He, B. Wang, Z. Han, J. Lu, K. Amine, H. Yu, In situ construction of uniform and robust cathode-electrolyte interphase for Li-rich layered oxides, Adv. Funct. Mater. 31 (8) (2020) 2009192, https://doi.org/10.1002/adfm.202009192.
[40] L. Zhang, F. Min, Y. Luo, G. Dang, H. Gu, Q. Dong, M. Zhang, L. Sheng, Y. Shen, L. Chen, J. Xie, Practical 4.4 V Li||NCM811 batteries enabled by a thermal stable and HF free carbonate-based electrolyte, Nano Energy 96 (2022) 107122. doi: 10.1016/j.nanoen.2022.107122.
[41] H.-H. Sun, A. Dolocan, J.A. Weeks, R. Rodriguez, A. Heller, C.B. Mullins, In situ formation of a multicomponent inorganic-rich SEI layer provides a fast charging and high specific energy Li-metal battery, J. Mater. Chem. A 7 (30) (2019) 17782–17789, https://doi.org/10.1039/c9ta05063a.
[42] Q. Li, X. Liu, X. Han, Y. Xiang, G. Zhong, J. Wang, B. Zheng, J. Zhou, Y. Yang, Identification of the solid electrolyte interface on the Si/C composite anode with FEC as the additive, ACS Appl. Mater. Interfaces 11 (15) (2019) 14066–14075, https://doi.org/10.1021/acsami.8b22221.
[43] G.-X. Li, H. Jiang, R. Kou, D. Wang, A. Nguyen, M. Liao, P. Shi, A. Silver, D. Wang, A superior carbonate electrolyte for stable cycling Li metal batteries using high Ni cathode, ACS Energy Lett. 7 (7) (2022) 2282–2288, https://doi.org/10.1021/acsenergylett.2c01090.
[44] Y. Wang, Separator wettability enhanced by electrolyte additive to boost the electrochemical performance of lithium metal batteries, Nano-Micro Lett. 13 (1) (2021) 210, https://doi.org/10.1007/s40820-021-00731-2.
[45] Y. Xie, H. Xiang, P. Shi, J. Guo, H. Wang, Enhanced separator wettability by LiTFSI and its application for lithium metal batteries, J. Membr. Sci. 524 (2017) 315–320, https://doi.org/10.1016/j.memsci.2016.11.021.
[46] M.-H. Ryou, D.J. Lee, J.-N. Lee, Y.M. Lee, J.-K. Park, J.W. Choi, Excellent Cycle life of lithium-metal anodes in lithium-ion batteries with mussel-inspired polydopamine-coated separators, Adv. Energy Mater. 2 (6) (2012) 645–650, https://doi.org/10.1002/aenm.201100687.
[47] Y. Fan, J. Liao, D. Luo, Y. Huang, F. Sun, J. Nan, In situ formation of a lithiophilic surface on 3D current collectors to regulate lithium nucleation and growth for dendrite-free lithium metal anodes, Chem. Eng. J. 453 (2023) 139903.
[48] A. Mohammadi, L. Monconduit, L. Stievano, R. Younesi, Measuring the nucleation overpotential in lithium metal batteries: never forget the counter electrode, J. Electrochem. Soc. 169 (7) (2022) 070509.
[49] A. Pei, G. Zheng, F. Shi, Y. Li, Y. Cui, Nanoscale nucleation and growth of electrodeposited lithium metal, Nano Lett. 17 (2) (2017) 1132–1139, https://doi.org/10.1021/acs.nanolett.6b04755.
[50] Z. Piao, P. Xiao, R. Luo, J. Ma, R. Gao, C. Li, J. Tan, K. Yu, G. Zhou, H.M. Cheng, Constructing a stable interface layer by tailoring solvation chemistry in carbonate electrolytes for high-performance lithium-metal batteries, Adv. Mater. 34 (8) (2022) e2108400.
[51] K. Hirata, Y. Morita, T. Kawase, Y. Sumida, Electrochemical performance of an ethylene carbonate-free electrolyte based on lithium bis(fluorosulfonyl)imide and sulfolane, J. Power Sources 395 (2018) 163–170, https://doi.org/10.1016/j.jpowsour.2018.05.059.
[52] S. Li, B. Li, X. Xu, X. Shi, Y. Zhao, L. Mao, X. Cui, Electrochemical performances of two kinds of electrolytes based on lithium bis(oxalate)borate and sulfolane for advanced lithium ion batteries, J. Power Sources 209 (2012) 295–300, https://doi.org/10.1016/j.jpowsour.2012.03.004.
[53] Q. Sun, Z. Cao, Z. Ma, J. Zhang, W. Wahyudi, T. Cai, H. Cheng, Q. Li, H. Kim, E. Xie, L. Cavallo, Y.-K. Sun, J. Ming, Discerning roles of interfacial model and solid electrolyte interphase layer for stabilizing antimony anode in lithium-ion batteries, ACS Mater. Lett. 4 (11) (2022) 2233–2243, https://doi.org/10.1021/acsmaterialslett.2c00679.
[54] Q. Zhao, Y. Wu, Z. Yang, D. Song, X. Sun, C. Wang, L.i. Yang, Y. Zhang, J. Gao, T. Ohsaka, F. Matsumoto, J. Wu, A fluorinated electrolyte stabilizing high-voltage graphite/NCM811 batteries with an inorganic-rich electrode-electrolyte interface, Chem. Eng. J. 440 (2022) 135939.
[55] P. Dai, X. Kong, H. Yang, S. Kuang, J. Zeng, J. Zhao, Synergistic effect of dual-anion additives promotes the fast dynamics and high-voltage performance of Ni-rich lithium-ion batteries by regulating the electrode/electrolyte interface, ACS Appl. Mater. Interfaces 14 (35) (2022) 39927–39938, https://doi.org/10.1021/acsami.2c08724.
[56] J. Zheng, M.H. Engelhard, D. Mei, S. Jiao, B.J. Polzin, J.-G. Zhang, W.u. Xu, Electrolyte additive enabled fast charging and stable cycling lithium metal batteries, Nat. Energy 2 (3) (2017), https://doi.org/10.1038/nenergy.2017.12.
[57] S. Ko, Y. Yamada, A. Yamada, An overlooked issue for high-voltage Li-ion batteries: suppressing the intercalation of anions into conductive carbon, Joule 5 (4) (2021) 998–1009, https://doi.org/10.1016/j.joule.2021.02.016.
[58] P. Xiao, R. Luo, Z. Piao, C. Li, J. Wang, K. Yu, G. Zhou, H.-M. Cheng, High-performance lithium metal batteries with a wide operating temperature range in carbonate electrolyte by manipulating interfacial chemistry, ACS Energy Lett. 6 (9) (2021) 3170–3179, https://doi.org/10.1021/acsenergylett.1c01528.
[59] R. Weber, M. Genovese, A.J. Louli, S. Hames, C. Martin, I.G. Hill, J.R. Dahn, Long cycle life and dendrite-free lithium morphology in anode-free lithium pouch cells enabled by a dual-salt liquid electrolyte, Nat. Energy 4 (8) (2019) 683–689, https://doi.org/10.1038/s41560-019-0428-9.